RGNZ/MGPB

Shallow subsurface structures and Quaternary deformations on the easternmost Matano fault, Indonesia, revealed by electrical resistivity tomography

Rudarsko-geološko-naftni zbornik
(The Mining-Geology-Petroleum Engineering Bulletin)
UDC: 550.8
DOI: 10.17794/rgn.2024.5.5

Original scientific paper

Adi Patria[1]; Muhammad Hanif[2]; Danny Hilman Natawidjaja[3]; Mudrik Rahmawan Daryono[4]

[1] *Research Centre for Geological Disaster, National Research and Innovation Agency (BRIN), Bandung, Indonesia, (ORCID: 0000-0002-9894-8443)*

[2] *Research Centre for Geological Disaster, National Research and Innovation Agency (BRIN), Bandung, Indonesia, (ORCID: 0000-0003-3702-6995)*

[3] *Research Centre for Geological Disaster, National Research and Innovation Agency (BRIN), Bandung, Indonesia, (ORCID: 0000-0002-3870-9184)*

[4] *Research Centre for Geological Disaster, National Research and Innovation Agency (BRIN), Bandung, Indonesia, (ORCID: 0000-0002-4052-1068)*

Abstract

In active fault studies, electrical resistivity tomography (ERT) with wide electrode spacing (10 m) and fewer than 60 electrodes is typically utilized. However, this configuration limits the ability of ERT to resolve detailed geological information, such as fault geometry and motion, small-scale offset, and thickness of Quaternary layers. High-resolution electrical resistivity tomography (ERT) with narrow electrode spacing (1.5–5 m) and 112 electrodes offers an opportunity to uncover finer geological information. This study combines ERT measurements with geological data from trenches and field observations to investigate the subsurface structures and Quaternary deformation on the easternmost Matano fault. On ERT sections, the easternmost Matano fault is characterized by deformed resistivity layers and resistivity contrasts. The subsurface fault structures dip steeply and indicate reverse and normal motions for the vertical component, with the displacement related to the Quaternary faulting ranging from 3 to 26 m. Notably, fault structures on ERT sections are not necessarily expressed by geomorphic features, suggesting obscured tectonic features. This study demonstrates the reliability of high-resolution electrical resistivity tomography (ERT) in unveiling geological information, such as fault location and geometry, fault vertical motions, buried fault structures, small-scale vertical offsets, stratigraphy, and Quaternary sediment thickness, which are essential for seismic hazard assessment.

Keywords:

active fault; Electrical resistivity tomography (ERT); Matano fault; seismic hazard; strike-slip fault

1. Introduction

Understanding the characteristics of active faults, such as location, geometry, motion, and small-scale displacements, is crucial for seismic hazard assessment. Electrical resistivity tomography (ERT) has been widely used to investigate the subsurface structures of active faults. However, applications of ERT in active fault studies are often limited by low-resolution data acquired using wide electrode spacing (e.g. 10 m) and a limited number of electrodes (fewer than 60) (e.g. **Fazzito et al., 2013; Peri et al., 2020; Sana et al., 2021**). Although this technique provides fast measurement, it limits the ability of ERT to image geological information in detail. Incorporating ERT with a configuration of narrower electrode spacing (≤ 5 m) and a more significant number of electrodes (112) would yield higher data resolution, enabling a more precise identification of geological features in the subsurface. Therefore, this study aims to test the reliability of ERT with a high-resolution configuration, as previously mentioned, to better characterize the shallow subsurface geology of active faults.

We present the results of the ERT measurement on the easternmost Matano fault in Sulawesi, Indonesia (see **Figure 1**), integrated with geological data from trenches and field observations. This fault portion was selected for two reasons. First, the fault traverses a Quaternary basin where its fault traces have been accurately mapped based on LiDAR (Light Detection and Ranging) DEM (Digital Elevation Model) in our previous work (i.e. **Patria et al., 2023**). Second, the Matano fault slips at a high rate of ~ 20 mm/yr (e.g. **Khairi et al., 2020; Patria et al., 2023; Walpersdorf et al., 1998**), which potentially records significant displacement in a relatively short period as well as displaying tectonic landscape evidence.

The left-lateral strike-slip Matano fault primarily accommodates the rapid westward motion of the Pacific

Corresponding author: Adi Patria
e-mail address: adip006@brin.go.id

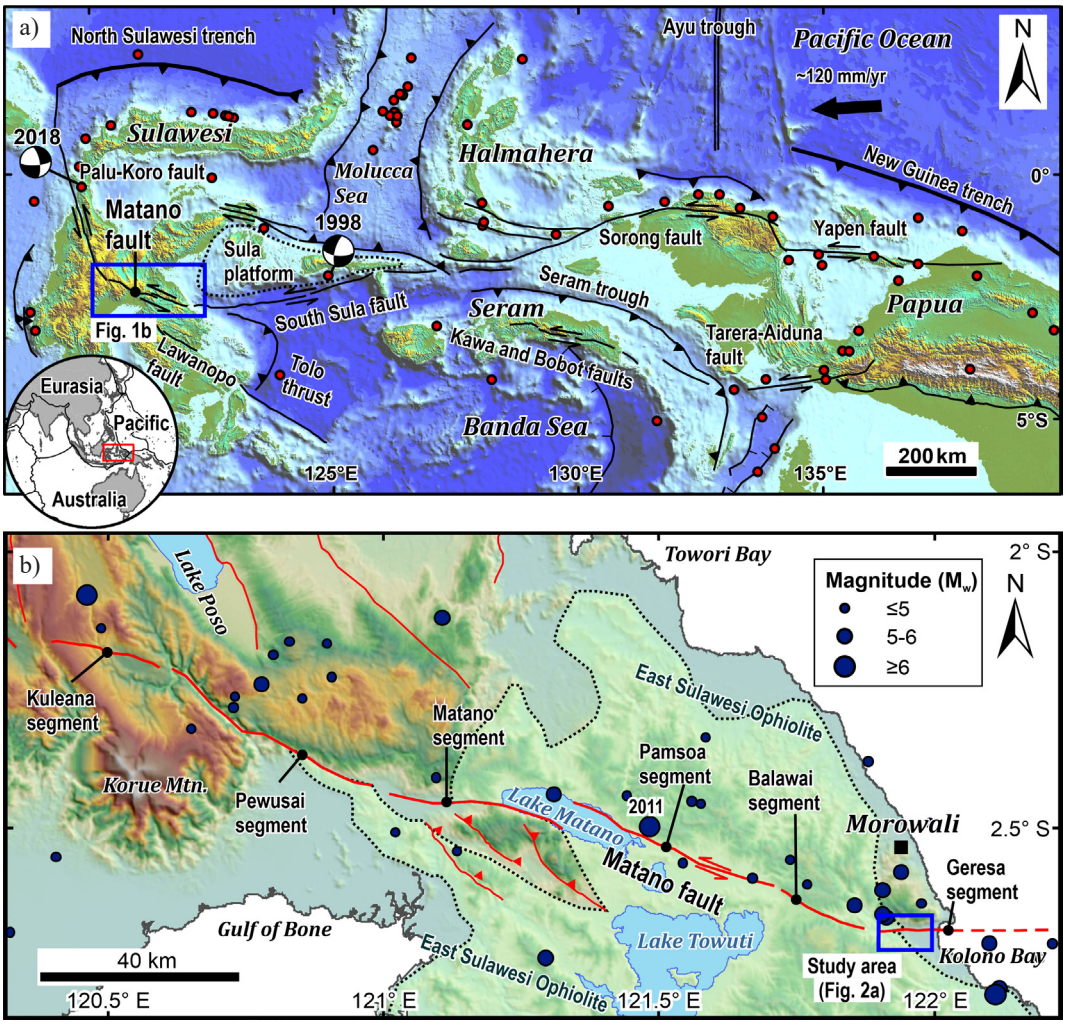

Figure 1: (a) Tectonic setting of eastern Indonesia (After **Hall, 2012; Patria et al., 2021; Pownall et al., 2016; Titu-Eki and Hall, 2020**). Red circles are earthquake hypocenters with Mw ≥7 and ≤40 km deep from the United States Geological Survey (USGS) earthquake catalog. **(b)** Fault traces and seismicity of the Matano fault (After **Center of National Earthquake Study (PuSGeN), 2017**). Blue circles are ≤40 km deep earthquake hypocenters from the USGS earthquake catalog.

Plate relative to the Australian Plate (**Bock et al., 2003; Socquet et al., 2006; Watkinson and Hall, 2017**) (see **Figure 1a**). The fault is located in the tropical region at a latitude of ~2°S, where surficial processes, such as erosion and sedimentation, are intense. Furthermore, the fault resides within the expansive East Sulawesi Ophiolite (see **Figure 1b**), acknowledged as one of the world's most significant ophiolites, encompassing an area exceeding 15,000 km^2 and extending for a length of 700 km (**Kadarusman et al., 2004; Monnier et al., 1995**). Several studies indicated that the Matano fault has the capability of generating Mw ≥7 earthquakes (e.g. **Center of National Earthquake Study (PuSGeN), 2017; Cipta et al., 2017; Daryono et al., 2021; Patria et al., 2023**). Therefore, the result of this investigation would also contribute to a seismic hazard evaluation of the Matano fault, particularly in the Morowali District, which has been developed as the ferronickel industrial zone.

2. Geological setting of the study area

This study focuses on the Larongsangi basin near Kolono Bay, a Quaternary basin at the eastern end of the Matano fault on land (see **Figures 1b** and **2a**). The basin is characterized by the presence of the Quaternary alluvium, for example, at locations 1 and 4 (see **Figures 2a, b** and **3a, b, e**), that unconformably overlies the basement rocks of the Triassic–Jurassic Tokala Formation and the Cretaceous Ultramafic Complex (**Simandjuntak et al., 1993**) (see **Figure 2a**). The Tokala Formation consists of clastic limestone that crops out in the mountainous terrain north of the basin, for example, at location 5 (see **Figures 2a, b,** and **3f**). The Cretaceous Ultramafic Complex occupies the mountainous region to the west and south, as indicated by serpentinite outcrops at locations 2 and 3 (see **Figures 2a, b** and **3c, d**).

Our previous work has precisely mapped the easternmost Matano fault's traces in the Larongsangi basin us-

Copyright held(s) by author(s), publishing rights belongs to publisher, pp. 75-88, DOI: 10.17794/rgn.2024.5.5

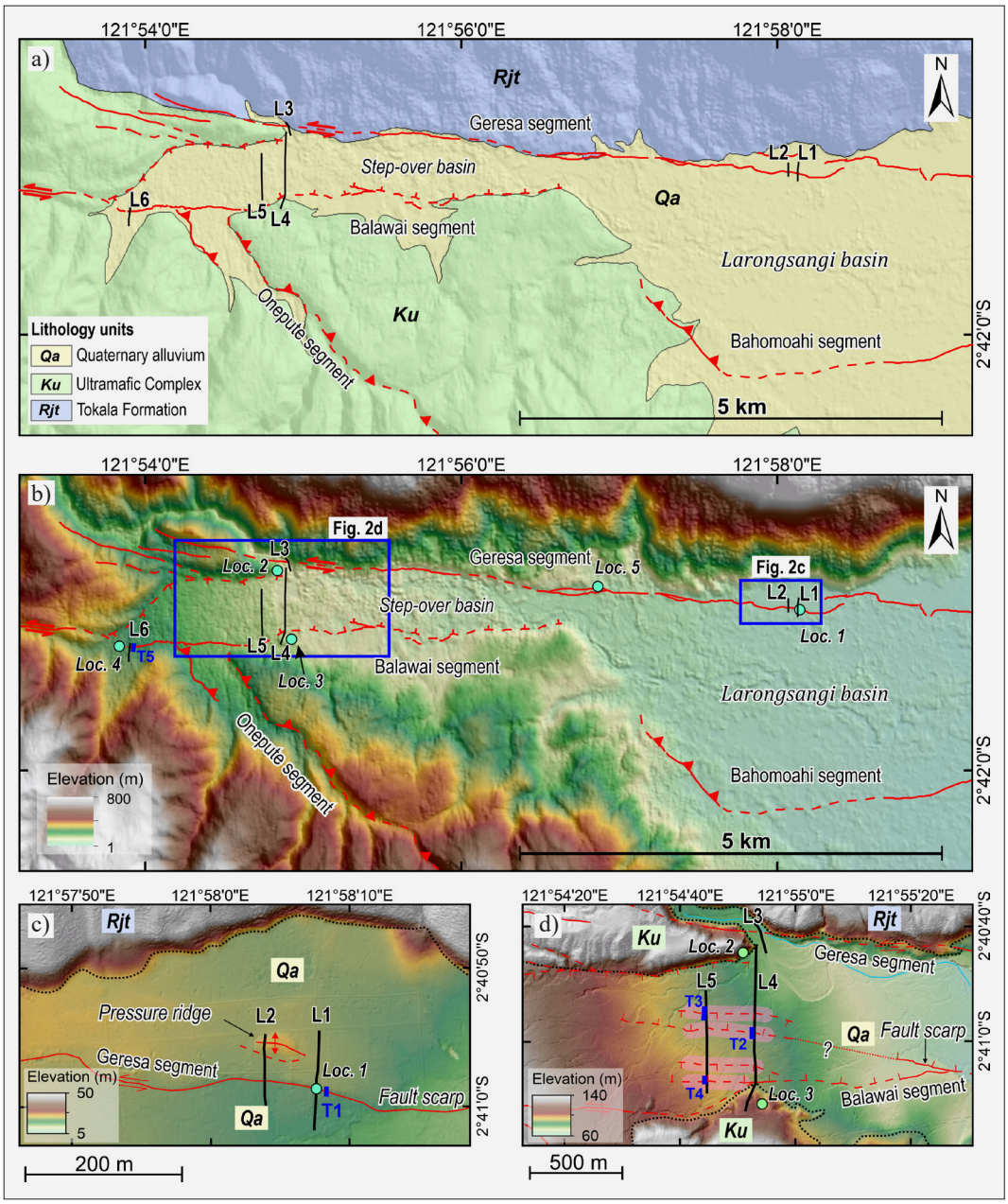

Figure 2: (**a**) Geological map of the study area with the surface traces of the Matano fault (After **Patria et al., 2023**; **Simandjuntak et al., 1993**). Black lines mark the ERT survey lines (L1–6). (**b**) Topography of the study area with the fault traces. A step-over basin is located between the Geresa and Balawai segments. (**c** and **d**) Detailed topography (LiDAR DEM) of selected areas around L1–2 and L3–5, respectively. Thick blue lines indicate the geological trenches. Faults highlighted pink in (d) were identified on ERT sections without prominent geomorphic expression.

ing LiDAR DEM data (**Patria et al., 2023**) (see **Figure 2**). The fault deforms the Quaternary deposit, suggesting its recent activity (see **Figure 3a, b, e**). The Geresa segment traverses along the northern margin of the basin and steps to the Balawai segment to the west. The step-over between the Geresa and Balawai segments manifests as a narrow step-over basin with a width of ~800 m. The Bahomoahi segment parallels the Geresa segment in the central part of the Larongsangi basin. Our paleoseismic investigation on the Geresa segment revealed that the easternmost Matano fault ruptured between the 15th and 19th centuries with an estimated Mw 7.4, and the recurrence interval of surface-rupturing earthquakes is calculated at 200–470 years (**Patria et al., 2023**).

3. Methodology

ERT, also known as georesistivity or geoelectric, is a near-surface geophysical technique that measures the resistivity of subsurface rocks by injecting electrical current into the subsurface through electrodes and measuring the resulting potential difference (**Telford et al., 1990**). The

Copyright held(s) by author(s), publishing rights belongs to publisher, pp. 75-88, DOI: 10.17794/rgn.2024.5.5

Figure 3: (**a**) Oblique photograph of the geomorphic setting of location 1 and lines L1–2. (**b**) 2 m high fault scarp on the Quaternary alluvium at location 1. (**c**) Fault cutting serpentinite (Ultramafic Complex) at location 2. (**d**) Serpentinite quarry at location 3. (**e**) 1 m high fault scarp on the Quaternary alluvium at location 4. (**f**) Limestone as river bed at location 5.

resolution and penetration depth depend on the distance between electrodes **(Loke and Dahlin, 2002; Storz et al., 2000)**; a wider distance between the electrodes results in greater penetration depth but decreases data resolution. Despite this trade-off, ERT surveys have been widely applied to investigate the subsurface structures of active faults, providing high-resolution, fast, and reliable results (e.g. **Daryono et al., 2019; Fazzito et al., 2013; Peri et al., 2020; Suzuki et al., 2000**).

In this study, we employed a high-resolution ERT configuration to image the shallow subsurface structures of the easternmost Matano fault within the Larongsangi basin. We utilized a multi-channel resistivity instrument, the *SuperSting IP R8* by *AGI USA* (see **Figure 4a**). The dipole-dipole configuration was selected for the acquisition due to its suitability for steeply-dipping faults, such as strike-slip faults (e.g. **Fazzito et al., 2013**) (see **Figure 4b**). We used 112 electrodes with spacing ranging from 1.5 to 5 m, depending on site accessibility and the targeted fault traces. The maximum penetration depth is approximately 24% of the section length. The horizontal resolution equals the electrode spacing, while the vertical resolution ranges from 0.3 to 1.7 times the electrode spacing. For example, 2 m electrode spacing yields a 222 m long section, a maximum depth of about 53 m, 2 m horizontal resolution, and ~0.6–3.4 m vertical resolution (see **Supplementary Figure 1**).

All section lines were oriented almost north-south, intersecting active fault traces (see **Figure 2**). In particular, the roll-along technique was applied during the acquisition of section L5 to obtain an extended continuous section, imaging the overall subsurface structure within the narrow step-over basin. The elevation differences along ERT lines were recorded using the *ZIPLEVEL PRO-2000* at every electrode position except for line L3, where the topography was relatively flat.

We used the *EarthImager 2D* software by *AGI USA* to process the resistivity data and produce the final inverted resistivity sections. The processing workflow includes topographic correction, model inversion, and forward modelling (see **Figure 4c**). We applied the finite-element method for the forward modelling and conducted up to 8 iterations to obtain the smallest RMS error. Then, we interpreted the final inverted resistivity sections by identifying distinct resistivity layers and faults. The layers were mainly differentiated based on their resistivity val-

Copyright held(s) by author(s), publishing rights belongs to publisher, pp. 75-88, DOI: 10.17794/rgn.2024.5.5

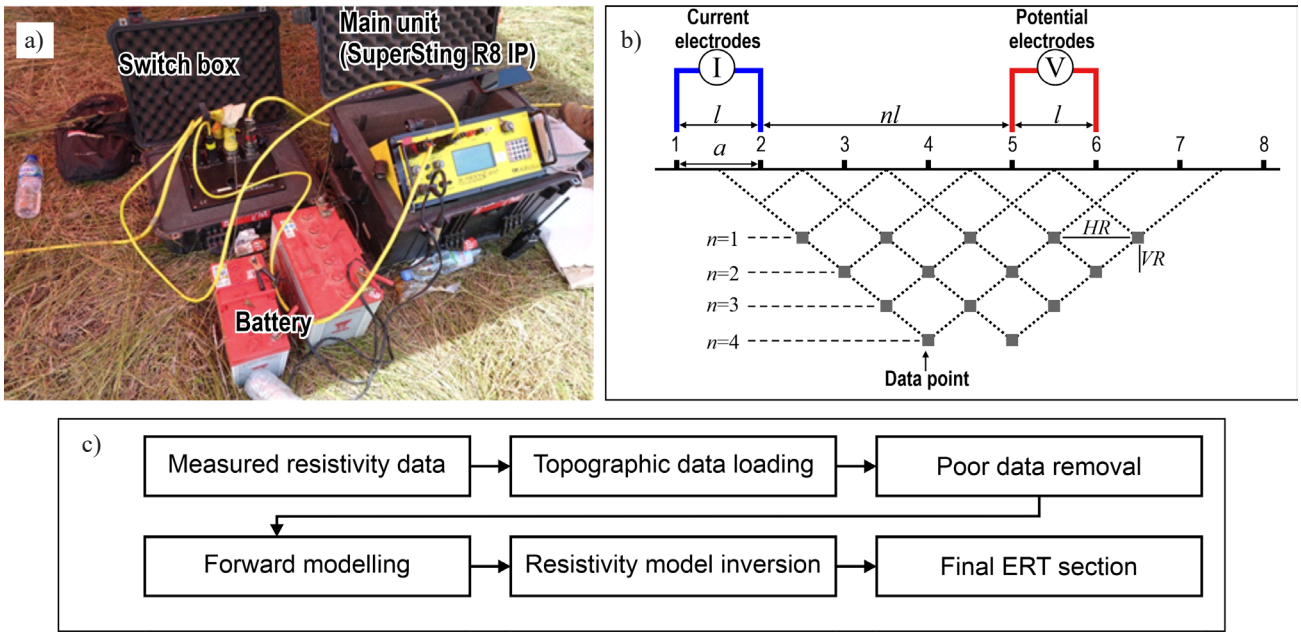

Figure 4: (**a**) ERT instrument used in this study, the *SuperSting IP R8*. (**b**) Dipole-dipole array configuration. *a* is the electrode spacing. *l* is the distance between pairs of current/potential electrodes, where *l* was set 1–6 times electrode spacing (*a*). *n* is the expansion factor. *HR* and *VR* are horizontal and vertical resolutions of data points, respectively. **(c)** Workflow of ERT data processing.

ues and stratigraphic positions. Faults on ERT sections manifested as displaced resistivity layers and lateral resistivity changes.

Furthermore, the resistivity layers and fault structures on the ERT sections were correlated with the geological information obtained in outcrops and trenches. We excavated five trenches, T1–5, to confirm the geological interpretation of the ERT sections. The trench walls were gridded and logged to record the geological information. A paleoseismic investigation with radiocarbon dating was done on trench T1, and the result has been published in Patria et al. (2023). We did not have an age constraint for layers observed on the other trenches, T2–5.

4. Results

This section describes the ERT sections and their geological interpretation from east to west. The raw data of ERT measurements and elevation profile are available at **URL 1**.

4.1. Sections L1 and L2

Lines L1 and L2 intersected a ~2-m-high south-facing fault scarp of the Geresa segment (see **Figure 2a–c**). Section L1 line was acquired near trench T1 (see **Figures 2c** and **3a**). Additionally, line L2 crossed a ~2.5-m-high pressure ridge (see **Figure 2c**). Three main resistivity layers and three faults were identified on sections L1 and L2 (see **Figure 5a, c**).

Layer A on section L1 is situated just beneath the surface and is characterized by a resistivity of 5–25 Ωm and a thickness of ~2–9 m (see **Figure 5a**). Within this layer, a local high resistivity anomaly reaches 130 Ωm (labeled HA on **Figure 5a**). Section L2 unveils a detailed stratification of layer A as layers A1–3 (see **Figure 5c**). Layer A1 exhibits a resistivity of 3–45 Ωm with a thickness of ~1 m. Below layer A1, the ~2 m thick layer A2 is indicated by a resistivity of 83–430 m. Layer A3 is characterized by lower resistivity than layer A2, down to 11 Ωm, with a thickness of ~6 m. Two localized low resistivity anomalies within layers A2 and A3 on section L2 (labeled LA on **Figure 5c**) disrupt these layers laterally below the pressure ridge, suggesting a non-sedimentary origin, probably related to liquefaction as sand boils (see **Figure 5d**). Based on trench T1 (see **Figure 6**), deformed sediments dated as Holocene (**Patria et al., 2023**) correlate layer A on section L1, pointing that the near-surface layers A and A1–3 correspond to the Quaternary alluvium (see **Figure 5b, d**). The pebble observed in trench T1 is considerably associated with the high resistivity anomaly on section L1 and was interpreted as a colluvial wedge developing at the fault scarp.

Layer B, below either layers A or A3, is characterized by a high resistivity reaching 1100 Ωm at its upper portion and a lower resistivity, 30 Ωm, at its lower part (see **Figure 5a, c**). Layer B was interpreted as the Ultramafic Complex (see **Figure 5b, d**) because the observations on section L4 (described in subsection 4.3), whose line intersected a serpentinite outcrop at location 3, suggests that the Ultramafic Complex in the study area is characterized by a combination of a high and low resistivity at the upper and lower portions, respectively. Layer B laterally discontinues to the north at fault F3, and a resistiv-

Copyright held(s) by author(s), publishing rights belongs to publisher, pp. 75-88, DOI: 10.17794/rgn.2024.5.5

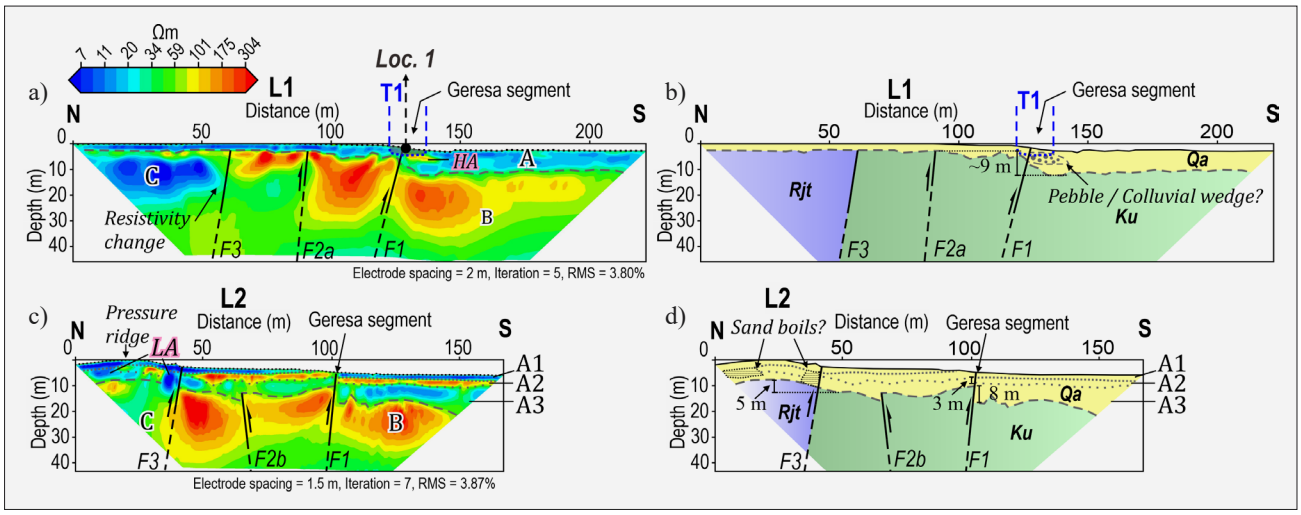

Figure 5: (**a**) Inverted resistivity section L1 with fault and layer delineations. Fault F1 corresponds to the Geresa segment's trace. (**b**) Subsurface geological interpretation of section L1 (see legend in **Figure 2a** for lithology units). (**c**) Inverted resistivity section L2 with fault and layer delineations. (**d**) Subsurface geological interpretation of section L2 (see legend in **Figure 2a** for lithology units).

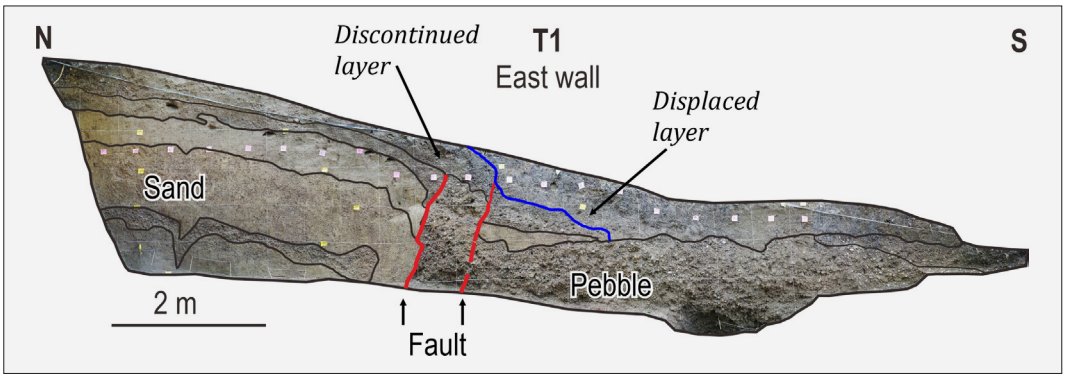

Figure 6: Photograph of trench T1 (east wall). The blue line marks the displaced layer.

ity of 3–150 Ωm defines layer C (see **Figure 5a, c**). Layer C is located beneath the pressure ridge on section L2. Layer C was interpreted as the Tokala Formation (see **Figure 5b, d**), composing the mountainous terrain north of lines L1 and L2 (see **Figure 2a**).

Fault F1 coincides with the Geresa segment's fault scarp and displaces layers A, A1–3, and B. Fault F1 steeply dips to the north, in agreement with the fault structures on trench T1 observed as discontinued and displaced layers (see **Figure 6**). The fault depicts a reverse motion component (see **Figure 5**). This motion on a north-dipping fault agrees with the south-facing fault scarp. The smallest offset on fault F1 is ~3 m on layer A2, ~1 m greater than the fault scarp's height of ~2 m (see **Figure 5d**). The difference between the fault scarp height and the vertical offset of layer A2, ~1 m, might represent the vertical displacement due to a single surface rupturing earthquake. The vertical offset calculated at the bottom of the Quaternary alluvium on sections L1 and L2 is ~9 m, much greater than the fault scarp's height, pronouncing the accumulative displacement due to repetitive surface-rupturing earthquakes on fault F1 or the Geresa segment (see **Figure 5b, d**).

On section L1, fault F2a was identified as a vertical offset of layer B below the undeformed portion of layer A (see **Figure 5a**). This observation suggests fault F2a is inactive because it does not disrupt the Quaternary layer. Fault F2b on section L2, which offset layer B, was also interpreted to be inactive as it does not disrupt layer A3 and above (see **Figure 5c**). Fault F3 is marked by a contrast resistivity change between layers B and C (see **Figure 5a, c**). Fault F3 does not deform layer A on section L1, while on section L2, it propagates till layer A1 and bounds the southern flank of the pressure ridge. This suggests that this fault might have been partly activated, forming the pressure ridge. This fault is also associated with the low resistivity anomaly near the surface (see **Figure 5c**).

4.2. Section L3

Section L3 was acquired on a relatively flat riverbank to assess the fault contact between the Tokala Formation and the Ultramafic Complex (see **Figure 2a, b, d**). The

Copyright held(s) by author(s), publishing rights belongs to publisher, pp. 75-88, DOI: 10.17794/rgn.2024.5.5

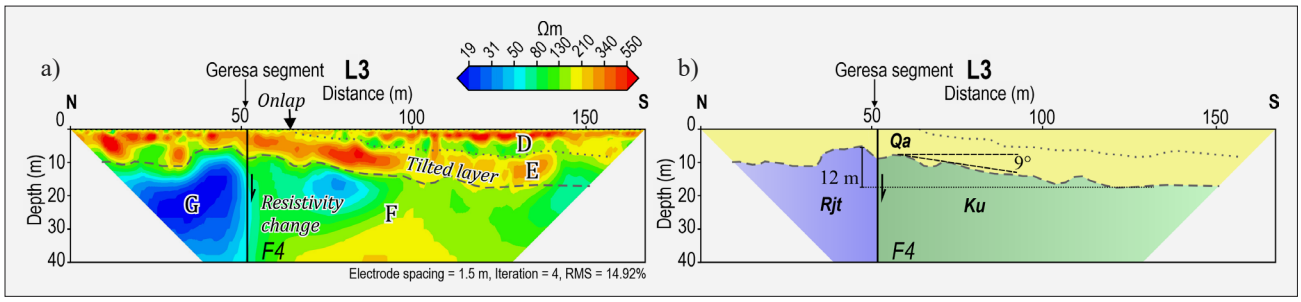

Figure 7: (**a**) Inverted resistivity section L3 with fault and layer delineations. Fault F4 corresponds to the Geresa segment's trace. (**b**) Subsurface geological interpretation of section L3 (see legend in **Figure 2a** for lithology units).

limestone outcrop at location 5 (see **Figures 2b** and **3f**) suggests that the high topography north of line L3 is composed of the Tokala Formation, while the serpentinite crops out at location 2 (see **Figures 2b, d,** and **3c**) indicates that the hill west of line L3 consists of the Ultramafic Complex. Section L3 illustrates four resistivity layers and a fault structure (see **Figure 7a**).

Layer D occupies the uppermost section from the distance of 65 m southward (see **Figure 7a**). This layer is marked by a resistivity value of 82 –1170 Ωm and thickens southward up to ~9 m. Layer E is situated partly below the surface at the distance of 0–65 m and partly below layer D to the south (see **Figure 7a**). The ~10 m thick layer E exhibits a resistivity of 170–1500 Ωm. It inclines at an angle of ~9° southward, starting at the distance of 52 m (see **Figure 7b**). Layers D and E represent the alluvial deposits on the riverbank where section L3 was acquired, classifying these layers into the Quaternary alluvium (see **Figure 7b**).

Layer F, with a resistivity of 35–220 Ωm, is located below the tilted portion of layer E (see **Figure 7a**). Below layer E at a distance of 0–50 m, layer G displays a lower resistivity than layer F, about 15–100 Ωm (see **Figure 7a**). Layer F was interpreted to correlate with the serpentinite outcrop at location 2, the Ultramafic Complex, while layer G likely corresponds to the Tokala Formation's limestone to the north (see **Figure 7b**). This observation pronounces that the Tokala Formation has a lower resistivity than the Ultramafic Complex, similar to the observation on sections L1 and L2.

Fault F4 is denoted by the lateral resistivity discontinuity between layers F and G and the tilting of layer E (see **Figure 7a**). This fault coincides with the beginning point of the tilt of layer E and the Geresa segment's trace interpretation by **Patria et al. (2023)**. This fault is almost vertical, and the tilted layer suggests that the vertical motion of the fault is down to the south. The vertical displacement is up to 12 m, calculated at the bottom of the Quaternary alluvium (see **Figure 7b**). This displacement is slightly larger than the vertical offset estimated for fault F1.

4.3. Sections L4 and L5

Sections L4 and L5 were acquired in the step-over basin between the Geresa and Balawai segments to reveal the fault pattern within the basin (see **Figure 2a, b, d**). Lines L4 and L5 were situated on the Quaternary alluvium, except the southernmost portion of line L4, which covers a piedmont consisting of the Ultramafic Complex as indicated by serpentinite at location 3 (see **Figures 2b, d,** and **3d**). Three resistivity layers and four faults were identified on these sections (see **Figures 8a** and **10a**).

Layer H is the uppermost layer on sections L4 and L5, characterized by a low resistivity of 5–10 Ωm in general and a resistivity reaching up to 2300 Ωm in places (see **Figures 8a** and **10a**). The thickness of this layer is ~12–20 m. Below layer H, layer I is indicated by a resistivity of 6–68 Ωm with a thickness of ~18–30 m (see **Figures 8a** and **10a**). As lines L4 and L5 mostly traverse the Quaternary alluvium (see **Figure 2a**), the near-surface layers H and I were interpreted as the alluvium (see **Figures 8b** and **10b**). Trenches T2–4 excavated within lines L4 and L5 above fault structures show that layer H is predominantly composed of gravel with a portion of sand (see **Figures 9** and **11**).

Below layer I, layer J is defined by a resistivity of 50–1600 Ωm at its upper portion and a resistivity of 25–50 Ωm at its lower portion (see **Figures 8a** and **10a**). A serpentinite outcrop at location 3 (see **Figures 2b** and **8a**) coincides with this layer at the surface on section L4, confirming that layer J constitutes the Ultramafic Complex (see **Figures 8b** and **10b**). This observation has been the basis for interpreting layer B on sections L1 and L2, layer F on section L3, and layer M on section L6.

Fault F5, the southernmost fault on sections L4 and L5, displaces layers H–J (see **Figures 8a** and **10a**). On section L4, this fault coincides with the Balawai segment at the surface. This fault steeply dips to the north and shows a down-to-the-north motion. On section L4, the vertical offset due to fault F5 is calculated at ~28 m at the bottom of the Quaternary layer (see **Figure 8b**). Section L5 shows a vertical offset of ~13 m at the top of layer I, and the offset becomes larger at the bottom of the Quaternary layer, ~18 m (see **Figure 10b**). In trench T4, fault F5 is indicated by a lithologic change between gravel and sand-gravel layers (see **Figure 11b**). North of fault F5, an antithetic fault F5', displaces layers H–J down to the south, with a vertical Quaternary displacement of ~23–31 m (see **Figures 8b** and **10b**).

Copyright held(s) by author(s), publishing rights belongs to publisher, pp. 75-88, DOI: 10.17794/rgn.2024.5.5

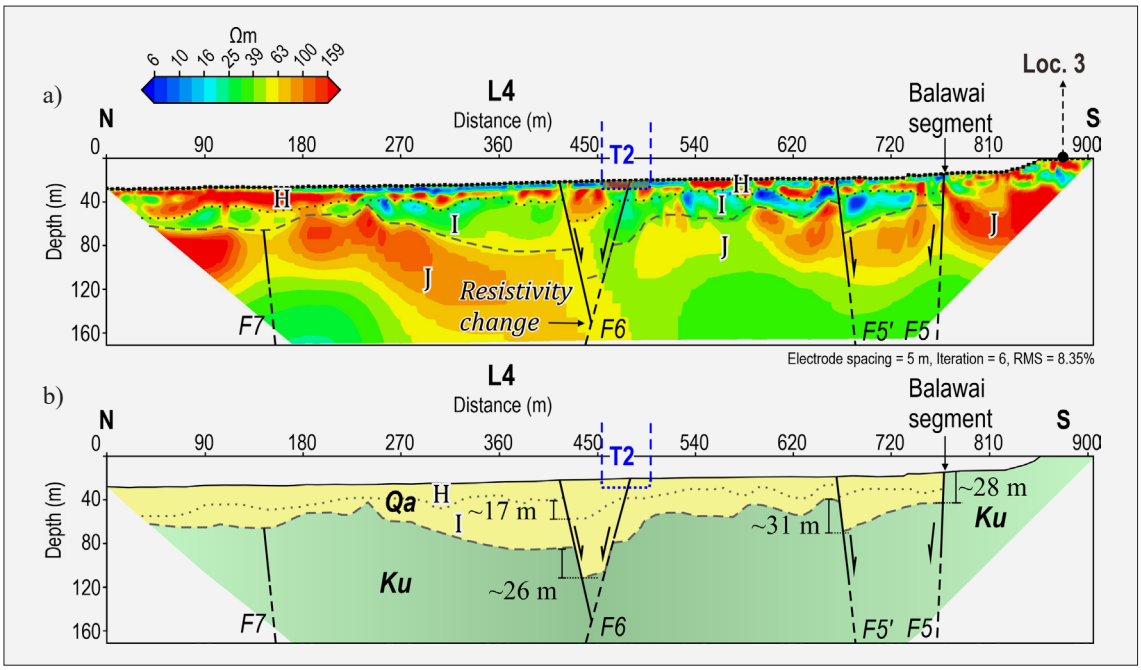

Figure 8: (**a**) Inverted resistivity section L4 with fault and layer delineations. Fault F5 corresponds to the Balawai segment's trace. (**b**) Subsurface geological interpretation of section L4 (see legend in **Figure 2a** for lithology units).

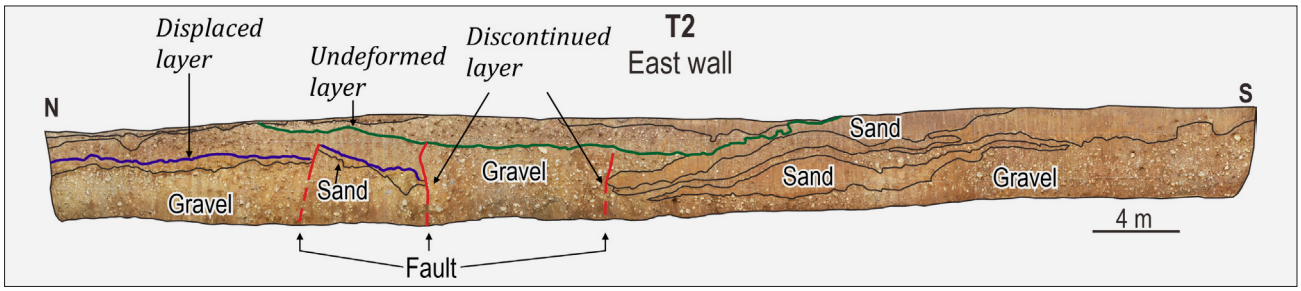

Figure 9: Photograph of trench T2 (east wall). Fault structures are overlain by the undeformed gravel layer (green line). The purple line marks the displaced layer.

Fault F6 was identified by displaced resistivity layers H–J on sections L4 and L5 (see **Figures 8a** and **10a**). This fault splays upward and forms a local graben where layers H and I become thicker. The vertical displacement of fault F6 reaches ~23–26 m, calculated at the bottom of the Quaternary alluvium (see **Figures 8b** and **10b**). The northern splay of fault F6 appears as sharp lateral changes between sand and gravel in trench T3 (see **Figure 11a**), and its southern splay is indicated by the vertically displaced sand layer and truncation of sedimentary layers in trench T2 (see **Figure 9**). On section L4, fault F7 was identified as a resistivity gap within layer J (see **Figure 8a**). Above this fault, layers H and I are not deformed, suggesting that this fault is inactive.

4.4. Section L6

Section L6 was measured above the Quaternary alluvium to examine the continuation of the Balawai segment to the west of section L5 (see **Figure 2a, b**). Just west of this section, at location 4, a 1 m fault scarp characterizes the Balawai segment (see **Figures 2b** and **3e**). This section exhibits three resistivity layers and a fault structure that branches upward (see **Figure 12a**).

The uppermost layer K exhibits a resistivity of 8–25 Ωm with an average thickness of ~3 m (see **Figure 12a**). Since section L6 was acquired above the Quaternary alluvium (see **Figure 2a**), layer K corresponds to this deposit (see **Figure 12b**). Based on trench T5, layer K is dominated by gravel with an intercalation of sand (see **Figure 13**). Below layer K, at the distance of 96–220 m, a resistivity value of 24–95 Ωm indicates layer L (see **Figure 12a**). This layer has a thickness of ~12 m and pinches out northward near the southern fault splay. The thinning of layer L suggests that a former topographic high plausibly limited its deposition in the past, developed due to the fault's motion. Layer M displays a resistivity value of 19–450 Ωm on this section, where its upper portion has a higher resistivity than its lower part (see **Figure 12a**). The resistivity of layer M resembles

Copyright held(s) by author(s), publishing rights belongs to publisher, pp. 75-88, DOI: 10.17794/rgn.2024.5.5

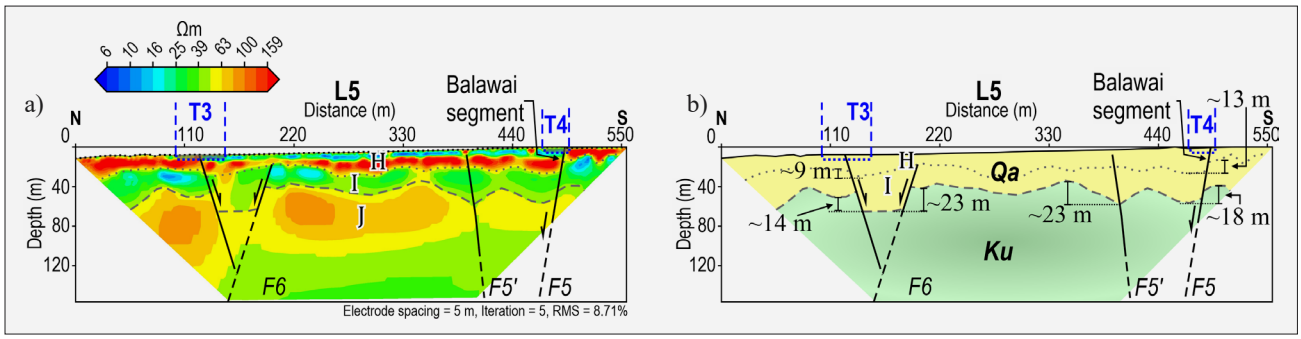

Figure 10: **(a)** Inverted resistivity section L5 with fault and layer delineations. Fault F5 corresponds to the Balawai segment's trace. **(b)** Subsurface geological interpretation of section L5 (see legend in **Figure 2a** for lithology units).

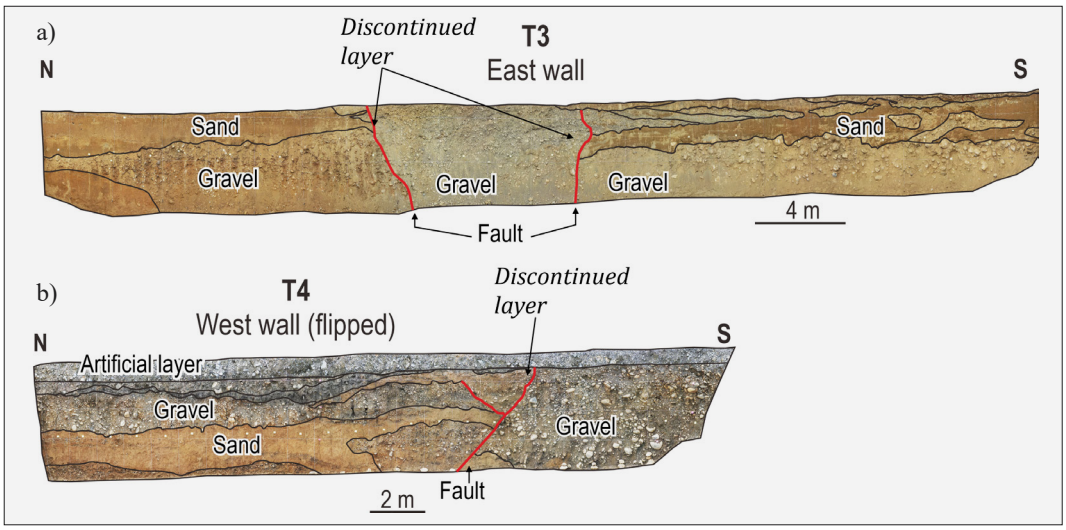

Figure 11: (**a** and **b**) Photograph of trenches T3 (east wall) and T4 (west wall), respectively

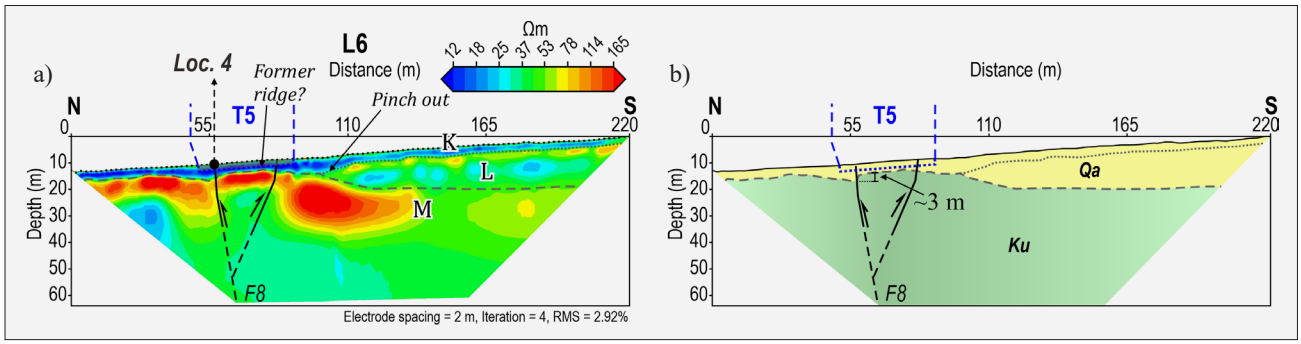

Figure 12: (**a**) Inverted resistivity section L6 with fault and layer delineations. Fault F8 corresponds to the Balawai segment's trace. (**b**) Subsurface geological interpretation of section L6 (see legend in **Figure 2a** for lithology units).

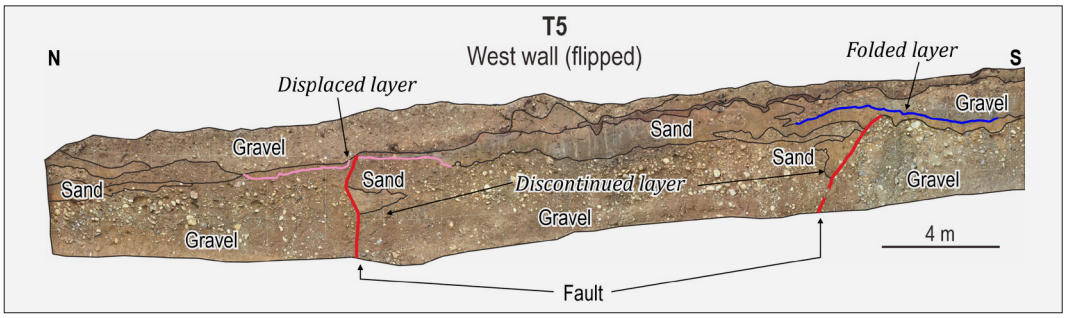

Figure 13: Photograph of trench T5 (west wall). Pink and blue lines mark the displaced and folded layers, respectively.

Copyright held(s) by author(s), publishing rights belongs to publisher, pp. 75-88, DOI: 10.17794/rgn.2024.5.5

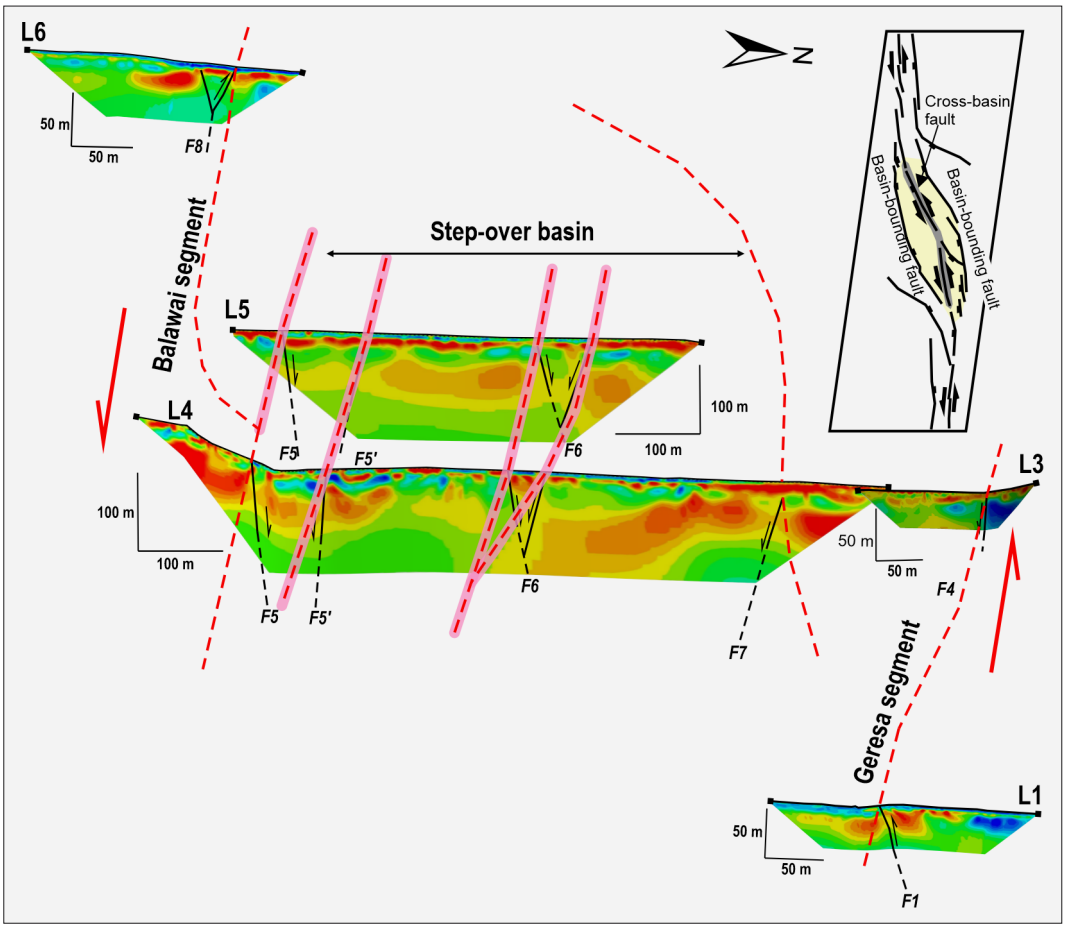

Figure 14: Schematic diagram illustrating the spatial correlation between faults identified on the ERT sections. The Geresa segment is expressed by faults F1 and F4, while the Balawai segment is represented by faults F5 and F8. Fault F6 is located within the step-over basin between the two segments. The Geresa and Balawai segments function as basin-bounding faults, while fault F6 was interpreted as a cross-basin fault. Thick pink lines highlight the faults identified based on ERT without prominent geomorphic expression. The upper right inset shows structural elements in a strike-slip basin based on an analog model by **Wu et al. (2009)**.

layer J on sections L4 and L5 and layer B on sections L1 and L2; hence, it was interpreted as the Ultramafic Complex (see **Figure 12b**).

The displacement of the upper portion of layer M at the distance of 55 and 91 m marks a pop-up structure as two oppositely-dipping fault splays, denoted as fault F8 (see **Figure 12a**). In trench T5, two fault structures were identified, representing both fault splays observed on section L6 (see **Figure 13**). The fault to the north is indicated by displaced layers, and the fault to the south is depicted by folded layers. The northern splay also correlates to the fault scarp at location 4 (see **Figure 12a**). The northern fault splay shows a vertical displacement of ~3 m, calculated at the bottom of the Quaternary layer (see **Figure 12b**).

5. Discussions

5.1. Reliability of high-resolution ERT

With the configuration used in this study, ERT effectively characterized the geometry of the easternmost Matano fault. Fault structures are constrained by displaced layers and resistivity contrasts. In some sections, the fault vertical motion could be determined; for example, the reverse motion of faults F1 and F8 and the normal motion of faults F5, F5, and F6. We were also able to calculate vertical offsets related to Quaternary deformation. Notably, using the electrode spacing of 1.5 m and 2 m allowed an identification of the vertical offset of ~3 m for layer A2 in section L2 and ~3 m for layer K in section L6. Furthermore, the ERT survey revealed obscured fault structures in sections L4 and L5 within the narrow step-over basin, confirmed by the trench observations.

Our high-resolution ERT allowed us to resolve finer details of the Quaternary layers, including thickness (minimum observed thickness is ~1 m for layer A1 in section L2 with 1.5 m electrode spacing), detailed layering, and geometry. Moreover, lateral variations within Quaternary layers, such as resistivity anomalies, could be identified, which might reflect variations in composition or fluid content related to the faulting activity, as

Copyright held(s) by author(s), publishing rights belongs to publisher, pp. 75-88, DOI: 10.17794/rgn.2024.5.5

exemplified by a high anomaly at fault F1 in section L1 and low anomalies at fault F3 in section L2.

The high-resolution ERT configuration used in this study successfully produced detailed subsurface images of the easternmost Matano fault. The rich geological information is helpful in seismic hazard assessment. For example, understanding the fault geometry and vertical motion is crucial because earthquakes would significantly impact the hanging wall block (the block above the fault). Identifying small-scale offsets would also help estimate the displacement of a single earthquake. In addition to the fault characteristics, the thickness of basin-filling sediments (Quaternary deposits) and the depth of the underlying basement rocks are essential parameters for calculating peak ground acceleration (PGA). Furthermore, identifying the location of obscured faults helps pinpoint the potential areas impacted by an earthquake surface rupture.

5.2. Fault geometry

The Matano fault is predominantly characterized by a left-lateral motion with a vertical-to-horizontal component ratio of 12–15% (**Patria et al., 2023**). Our observation on the ERT sections indicates that the fault is characterized by subvertical–vertical fault planes with both reverse and normal slips as the vertical component (see **Figure 14**). The fault structures observed in trenches agree with the faults identified on the ERT sections. Displaced near-surface resistivity layers, which are correlated with the young sediments exposed in the trenches, express the fault's Quaternary activity.

Sections L1 and L2 depict the reverse motion component of the Geresa segment (see **Figure 5**). The faults in these sections indicate the contractional component of the deformation on the Geresa segment. The north dipping fault F1 aligned with the Geresa segment's fault scarp is correlated with the fault structures observed in trench T1. Section L2 illustrates the subsurface structure of a pressure ridge where the subsidiary fault F3 controls the ridge's formation. In contrast, section L3 reveals that the south-dipping fault F4 with a normal motion component represents the Geresa segment (see **Figure 7**). The observations on sections L1–3 reveal that the Geresa segment consists of both north- and south-dipping fault planes with reverse and normal motion components, respectively.

Within the step-over basin, sections L4 and L5 illustrate faults with a normal motion component (see **Figures 8** and **10**). The structural pattern within the step-over basin suggests a negative flower structure related to a restraining step-over between the Geresa and Balawai segments. The north-dipping fault F5 coincides with the trace of the Balawai segment. Fault F6, situated in the middle of the strike-slip basin, exhibits considerable vertical motion, although it does not correlate with any surficial geomorphic feature. Trenches T2 and T3, excavated at fault F6, clearly provide evidence of its Quaternary activity. On section L6, the Balawai segment is represented by fault F8, forming a pop-up structure and suggesting a contractional partition on the Balawai segment (see **Figure 12**).

Faults F1 and F4 are consistent with the geomorphology of the Geresa segment, while faults F5 and F8 align with the Balawai segment's traces (see **Figure 14**). Therefore, we interpreted these faults as the main structures of the Matano fault in the study area. The Geresa and Balawai segments exhibit along-strike variations in vertical motion, a typical feature observed on strike-slip faults. This variation could be attributed to bends or steps, causing localized uplift or subsidence.

In the context of a strike-slip basin, the Geresa and Balawai segments can be regarded as basin-bounding faults, causing the formation of a basin at their restraining step-over (see **Figure 14**). The Quaternary alluvium correlated with the near-surface layers has a thickness of ~10–50 m (see **Figure 15**). The maximum thickness of this alluvium is observed in the step-over basin, precisely at the graben structure of fault F6 in section L4 (see **Figure 8**). This observation suggests that the step-over basin functions as a depocenter between the Geresa and Balawai segments. The intra-basin fault F6 was interpreted as a cross-basin fault, which often develops during the later stages of basin development due to the tendency of strike-slip faults to straighten (**Wu et al., 2009**). This fault accommodates a significant portion of the

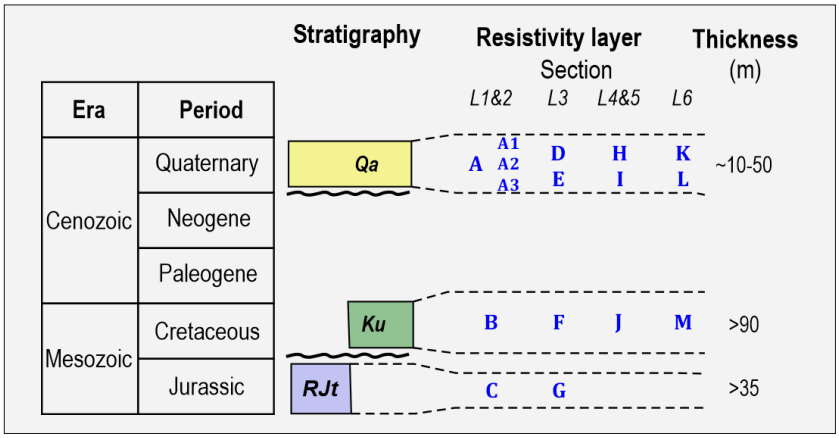

Figure 15: Correlation between the geological formations and the resistivity layers identified on the ERT sections. *Qa*: Quaternary alluvium; *Ku*: Ultramafic Complex; *RJt*: Tokala Formation.

strike-slip movement (**Wu et al., 2009**). If this is the case, fault F6 should have a prominent surface expression. However, the geomorphic expression associated with fault F6 is absent, possibly due to intense erosion and sedimentation in the step-over basin, which could quickly remove the fault's surface expression.

5.3. Seismic hazard

The Matano fault's Quaternary activity is evidenced by the displaced near-surface resistivity layers, interpreted as the Quaternary alluvium. Radiocarbon dating of sedimentary layers in trench T1 revealed an age between the 10th and 20th centuries (**Patria et al., 2023**). Since these sediments correlate with layer A on section L1, layer A can be classified as young or Holocene. Similarly, other uppermost layers (A1, D, H, and K) are likely Holocene deposits. Therefore, faults F1, F3, F4, F5, F5', F6, and F8, which deform the uppermost layers, might have been activated during the most recent surface-rupturing earthquake. Our previous study proposed that the most recent surface-faulting event might have simultaneously ruptured a 110-km-long eastern portion of the Matano fault, including the Geresa and Balawai segments (**Patria et al., 2023**). Additionally, the low resistivity anomalies observed in section L2 (see **Figure 5c, d**) suggest lateral stratigraphic disturbances, possibly related to liquefaction triggered by past earthquakes.

The identification of obscured faults F5'and F6 in the step-over basin is important for accurate seismic hazard evaluation. Specifically, the cross-basin fault F6 might accommodate most of the slip during surface-rupturing earthquakes. This is exemplified by the 2018 Mw 7.5 Palu-Koro earthquake in Sulawesi, Indonesia, which ruptured cross-basin faults lacking surface expression within the pull-apart Palu basin (e.g. **Komura and Sugimoto, 2021; Natawidjaja et al., 2021; Patria and Putra, 2020**). Thus, identifying the location of cross-basin faults could anticipate the impact of earthquake surface rupture in strike-slip basins.

5.4. Geological implication

Our interpretation of the ERT sections enables us to establish a correlation between the resistivity layers and the geological formations in the study area (see **Figure 15**). The near-surface layers on ERT sections, indicated by various resistivity values spanning from 3 to 2300 Ωm, comprise gravel and sand deposits of the Quaternary alluvium. The thickness of the alluvium ranges from 10 to 50 m. The Tokala Formation, as indicated by a relatively low resistivity (≤150 Ωm) below the Quaternary layers, is in fault contact with the Ultramafic Complex. The Ultramafic Complex is characterized by a combination of an up-to-40-m thick high resistivity value of 40–1600 Ωm at its upper portion and a low resistivity of ≤50 Ωm at its lower part.

The contact between the Ultramafic Complex and Tokala Formation, as evident in sections L1–3, was interpreted as the Matano fault (see **Figures 5** and **7**). This fault is a result of the collision between Sulawesi and the Sula platform during the middle Pliocene (**Villeneuve et al., 2002**) (see **Figure 1a** for location reference), which has uplifted the Triassic–Jurassic Tokala Formation, truncating the younger Cretaceous Ultramafic Complex. The Matano fault has remained active since then and now deforms the Quaternary alluvium.

6. Conclusions

We have conducted ERT measurements with a high-resolution configuration of 1.5–5 m electrode spacing and 112 electrodes to investigate the subsurface structures of the easternmost Matano fault in the Larongsangi basin. This configuration is effective for imaging detailed subsurface features associated with the fault, including locations, geometry, motions, small-scale vertical offsets, stratigraphy, and sedimentary thickness. The resistivity layers and fault structures identified on the ERT sections correlate well with the geological information from trenches and field observation. Moreover, this ERT configuration can identify obscured fault structures within a basin. The vertical offset calculated on the ERT section ranges from 3 to 26 m, representing the Quaternary deformation of the fault. Our results demonstrate the potential application of the ERT method with narrow electrode spacing and a large number of electrodes for detailed characterization of active faults.

The ERT sections depict the Matano fault's subsurface structures as deformed and discontinuous resistivity layers. Deformed near-surface resistivity layers indicate the fault's quaternary activity. This fault exhibits steeply dipping planes and displays reverse and normal motions as the vertical component. Furthermore, we identified an obscured cross-basin fault in the narrow step-over basin between the Geresa and Balawai segments.

Acknowledgement

We thank Nyanjang, Nandang Supriatna, Sutarman, and Bambang Widoyoko Suwargadi for the field assistance. Hiroyuki Tsutsumi is thanked for the supervision of AP's PhD study. Ilham Arisbaya is thanked for the discussion on methodology. The field survey received support and facilitation from PT. Ground Risk Management and PT. Aquila-Solway, particularly Simon Ballantyne and Nikita Novikov. AP was funded by the MEXT Scholarship from the Japanese Government for his PhD study at Doshisha University. This study was also supported by the Royal Society, UK (Grant No. CHL\R1\180173) and the 2023 Disaster Research Grant Program (Rumah Program Kebencanaan 2023) from the Research Organization for Earth Sciences and Maritime, National Research and Innovation Agency of Indonesia

Copyright held(s) by author(s), publishing rights belongs to publisher, pp. 75-88, DOI: 10.17794/rgn.2024.5.5

(BRIN) (Grant No. 2/III.4/HK/2023). Finally, we thank Tomislav Korman and Zoran Kovač for their editorial handling and three anonymous reviewers for their comments, which significantly improved this manuscript.

7. References

Bock, Y., Prawirodirdjo, L., Genrich, J.F., Stevens, C.W., McCaffrey, R., Subarya, C., Puntodewo, S.S.O., Calais, E., (2003): Crustal motion in Indonesia from Global Positioning System measurements. Journal of Geophysical Research: Solid Earth, 108, 2367. https://doi.org/10.1029/2001jb000324

Center of National Earthquake Study (PuSGeN), (2017): Earthquake sources and hazards map of Indonesia 2017 (Peta Sumber dan Bahaya Gempa Indonesia Tahun 2017). Pusat Penelitian dan Pengembangan Perumahan dan Permukiman, Bandung. (in Indonesian).

Cipta, A., Robiana, R., Griffin, J.D., Horspool, N., Hidayati, S., Cummins, P.R., (2017): A probabilistic seismic hazard assessment for Sulawesi, Indonesia, in: Cummins, P.R., Meilano, I. (Eds.), Geohazards in Indonesia: Earth Science for Disaster Risk Reduction. Geological Society of London, London, pp. 133–152. https://doi.org/10.1144/SP441.6

Daryono, M.R., Kumarawarman, B., Muslim, I.H., Triwurjani, R., Permadi, R., Prihatmoko, S., Wibowo, S., Tutuko, G.H., (2021): Two earthquake events on the Pamsoa Segment of the Matano Fault, Sulawesi. IOP Conference Series: Earth and Environmental Science, 873, 12053. https://doi.org/10.1088/1755-1315/873/1/012053

Daryono, M.R., Natawidjaja, D.H., Sapiie, B., Cummins, P., (2019): Earthquake Geology of the Lembang Fault, West Java, Indonesia. Tectonophysics 751, 180–191. https://doi.org/10.1016/j.tecto.2018.12.014

Fazzito, S.Y., Cortés, J.M., Rapalini, A.E., Terrizzano, C.M., (2013): The geometry of the active strike-slip El Tigre Fault, Precordillera of San Juan, Central-Western Argentina: Integrating resistivity surveys with structural and geomorphological data. International Journal of Earth Sciences, 102, 1447–1466. https://doi.org/10.1007/s00531-013-0873-9

Hall, R., (2012): Late Jurassic-Cenozoic reconstructions of the Indonesian region and the Indian Ocean. Tectonophysics 570–571, 1–41. https://doi.org/10.1016/j.tecto.2012.04.021

Kadarusman, A., Miyashita, S., Maruyama, S., Parkinson, C.D., Ishikawa, A., (2004): Petrology, geochemistry and paleogeographic reconstruction of the East Sulawesi Ophiolite, Indonesia. Tectonophysics 392, 55–83. https://doi.org/https://doi.org/10.1016/j.tecto.2004.04.008

Khairi, A., Awaluddin, M., Sudarsono, B., (2020): Analysis of Seismic Deformation on the Matano fault using GNSS and SAR interferometric (Analisis Deformasi Seismik Sesar Matano Menggunakan GNSS dan Interferometrik SAR). Jurnal Geodesi Undip, 9, 32-42. (in Indonesian with English abstract). https://doi.org/10.14710/jgundip.2020.27163

Komura, K., Sugimoto, J., (2021): Shortcut Faults and Lateral Spreading Activated in a Pull-Apart Basin by the 2018 Palu Earthquake, Central Sulawesi, Indonesia. Remote Sens. https://doi.org/10.3390/rs13152939

Loke, M.H., Dahlin, T., (2002): A comparison of the Gauss-Newton and quasi-Newton methods in resistivity imaging inversion. Journal of Applied Geophysics, 49, 149–162. https://doi.org/10.1016/S0926-9851(01)00106-9

Monnier, C., Girardeau, J., Maury, R.C., Cotten, J., (1995): Back-arc basin origin for the East Sulawesi ophiolite (eastern Indonesia). Geology 23, 851–854. https://doi.org/10.1130/0091-7613(1995)023<0851:BABOFT>2.3.CO;2

Natawidjaja, D.H., Daryono, M.R., Prasetya, G., Liu, P.L.-F., Hananto, N.D., Kongko, W., Triyoso, W., Puji, A.R., Meilano, I., Gunawan, E., Supendi, P., Pamumpuni, A., Irsyam, M., Faizal, L., Hidayati, S., Sapiie, B., Kusuma, M.A., Tawil, S., (2021): The 2018 Mw7.5 Palu 'supershear' earthquake ruptures geological fault's multisegment separated by large bends: results from integrating field measurements, LiDAR, swath bathymetry and seismic-reflection data. Geophysical Journal International, 224, 985–1002. https://doi.org/10.1093/gji/ggaa498

Patria, A., Natawidjaja, D.H., Daryono, M.R., Hanif, M., Puji, A.R., Tsutsumi, H., (2023): Tectonic landform and paleoseismic events of the easternmost Matano fault in Sulawesi, Indonesia. Tectonophysics 852, 229762. https://doi.org/10.1016/j.tecto.2023.229762

Patria, A., Putra, P.S., (2020): Development of the Palu–Koro Fault in NW Palu Valley, Indonesia. Geoscience Letters, 7, 1. https://doi.org/10.1186/s40562-020-0150-2

Patria, A., Tsutsumi, H., Natawidjaja, D.H., (2021): Active fault mapping in the onshore northern Banda Arc, Indonesia: Implications for active tectonics and seismic potential. Journal of Asian Earth Sciences, 218, 104881. https://doi.org/https://doi.org/10.1016/j.jseaes.2021.104881

Peri, V.G., Rapalini, A.E., Pérez, P., Franceschinis, P., Leiva, M.F., Fazzito, S.Y., Cortés, J.M., (2020): Subsurface characterization of quaternary scarps and their possible connection to main structures of the western margin of Precordillera, San Juan, Argentina. Tectonophysics 790, 228542. https://doi.org/10.1016/j.tecto.2020.228542

Pownall, J.M., Hall, R., Lister, G.S., (2016): Rolling open Earth's deepest forearc basin. Geology 44, 947–950. https://doi.org/10.1130/G38051.1

Sana, H., Taborik, P., Valenta, J., Bhat, F.A., Flašar, J., Štěpančíkova, P., Khwaja, N.A., (2021): Detecting active faults in intramountain basins using electrical resistivity tomography: A focus on Kashmir Basin, NW Himalaya. Journal of Applied Geophysics, 192, 104395. https://doi.org/https://doi.org/10.1016/j.jappgeo.2021.104395

Simandjuntak, T.O., Rusmana, E., Supandjono, J.B., Koswara, A., (1993): Geological map of Bungku quadrangle, Sulawesi. Geological Research and Development Centre, Bandung.

Socquet, A., Simons, W., Vigny, C., McCaffrey, R., Subarya, C., Sarsito, D., Ambrosius, B., Spakman, W., (2006): Microblock rotations and fault coupling in SE Asia triple junction (Sulawesi, Indonesia) from GPS and earthquake slip vector data. Journal of Geophysical Research: Solid Earth, 111, B08409. https://doi.org/10.1029/2005JB003963

Copyright held(s) by author(s), publishing rights belongs to publisher, pp. 75-88, DOI: 10.17794/rgn.2024.5.5

Storz, H., Storz, W., Jacobs, F., (2000): Electrical resistivity tomography to investigate geological structures of the earth's upper crust. Geophysical Prospecting, 48, 455–471. https://doi.org/10.1046/j.1365-2478.2000.00196.x

Suzuki, K., Toda, S., Kusunoki, K., Fujimitsu, Y., Mogi, T., Jomori, A., (2000): Case studies of electrical and electromagnetic methods applied to mapping active faults beneath the thick quaternary. Developments in Geotechnical Engineering, 84, 29–45. https://doi.org/10.1016/S0165-1250(00)80005-X

Telford, William Murray, Telford, W M, Geldart, L.P., Sheriff, R.E., (1990): Applied geophysics. Cambridge university press.

Titu-Eki, A., Hall, R., (2020): The Significance of the Banda Sea: Tectonic Deformation Review in Eastern Sulawesi. Indonesian Journal on Geoscience, 7, 291–303. https://doi.org/10.17014/ijog.7.3.291-303

URL 1: https://hdl.handle.net/20.500.12690/RIN/4PKHXA.

Villeneuve, M., Gunawan, W., Cornee, J.-J., Vidal, O., (2002): Geology of the central Sulawesi belt (eastern Indonesia): constraints for geodynamic models. International Journal of Earth Sciences, 91, 524–537. https://doi.org/10.1007/s005310100228

Walpersdorf, A., Vigny, C., Manurung, P., Subarya, C., Sutisna, S., (1998): Determining the Sula block kinematics in the triple junction area in Indonesia by GPS. Geophysical Journal International, 135, 351–361. https://doi.org/10.1046/j.1365-246X.1998.00641.x

Watkinson, I.M., Hall, R., (2017): Fault systems of the eastern Indonesian triple junction: evaluation of Quaternary activity and implications for seismic hazards, in: Cummins, P.R., Meilano, I. (Eds.), Geohazards in Indonesia: Earth Science for Disaster Risk Reduction. Geological Society of London, London, pp. 71–120. https://doi.org/10.1144/SP441.8

Wu, J.E., McClay, K., Whitehouse, P., Dooley, T., (2009): 4D analogue modelling of transtensional pull-apart basins. Marine and Petroleum Geology, 26, 1608–1623. https://doi.org/10.1016/j.marpetgeo.2008.06.007

SAŽETAK

Plitke potpovršinske strukture i deformacije kvartarnih naslaga otkrivene metodom električne tomografije na najistočnijemu dijelu rasjeda Matano, Indonezija

U istraživanjima aktivnih rasjeda obično se koristi metoda električne tomografije (ERT) sa širokim razmakom elektroda (10 m) i manje od 60 elektroda. Međutim, ova konfiguracija ograničava mogućnosti električne tomografije u razlučivanju detaljnih geoloških informacija, kao što su geometrija rasjeda i kretanje, mali pomaci i debljina kvartarnih naslaga. Električna tomografija visoke rezolucije s malim razmakom elektroda (1,5 – 5 m) i 112 elektroda nudi priliku za otkrivanje detaljnijih geoloških struktura. U okviru ove studije metoda električne tomografije korištena je u kombinaciji s geološkim podatcima iz rovova i zapažanjima na terenu kako bi se istražile potpovršinske strukture i deformacije kvartarnih naslaga na najistočnijemu dijelu rasjeda Matano. Na profilima električne tomografije najistočniji dio rasjeda karakteriziraju deformirani slojevi otpornosti kao i kontrasti u otpornosti. Potpovršinske rasjedne strukture strmo su nagnute te upućuju na reverzne i normalne rasjede s vertikalnim pomakom od 3 do 26 m koji se odnosi na rasjedanje u kvartarnim naslagama. Primjetno je i da rasjedne strukture na profilima električne tomografije nisu nužno izražene u geomorfološkim značajkama, što upućuje na prikrivene tektonske značajke. Ova studija pokazuje pouzdanu primjenu električne tomografije visoke rezolucije u otkrivanju detaljnih geoloških informacija, kao što su lokacija i geometrija rasjeda, vertikalna gibanja rasjeda, prekrivene rasjedne strukture, mali vertikalni pomaci, stratigrafija te debljina kvartarnih naslaga, a koji su bitni za procjenu seizmičkoga hazarda.

Ključne riječi:
aktivan rasjed, električna tomografija, seizmički hazard, *strike-slip* rasjed

Author's contributions

Adi Patria (1) (Dr., Researcher, Earthquake Geology) who processed and interpreted the ERT sections, analyzed the results, and wrote the original manuscript. **Muhammad Hanif (2)** (M.Sc., Researcher, Near-surface Geophysics) processed ERT sections and provided a discussion for ERT interpretation. **Danny Hilman Natawidjaja (3)** (PhD, Research Professor, Earthquake Geology) led and supervised the study and provided a discussion for ERT interpretation. **Mudrik Rahmawan Daryono (4)** (Dr., Senior Researcher, Earthquake Geology) provided a discussion for ERT interpretation. All authors participated in the field survey and read, reviewed, and approved the final manuscript.

Copyright held(s) by author(s), publishing rights belongs to publisher, pp. 75-88, DOI: 10.17794/rgn.2024.5.5